

EchoFlow: A Foundation Model for Cardiac Ultrasound Image and Video Generation

Hadrien Reynaud, Alberto Gomez, Paul Leeson, Qingjie Meng*, and Bernhard Kainz*, *Senior Member, IEEE*

Abstract—Advances in deep learning have significantly enhanced medical image analysis, yet the availability of large-scale medical datasets remains constrained by patient privacy concerns. We present EchoFlow, a novel framework designed to generate high-quality, privacy-preserving synthetic echocardiogram images and videos. EchoFlow comprises four key components: an adversarial variational autoencoder for defining an efficient latent representation of cardiac ultrasound images, a latent image flow matching model for generating accurate latent echocardiogram images, a latent re-identification model to ensure privacy by filtering images anatomically, and a latent video flow matching model for animating latent images into realistic echocardiogram videos conditioned on ejection fraction. We rigorously evaluate our synthetic datasets on the clinically relevant task of ejection fraction regression and demonstrate, for the first time, that downstream models trained exclusively on EchoFlow-generated synthetic datasets achieve performance parity with models trained on real datasets. We release our models and synthetic datasets, enabling broader, privacy-compliant research in medical ultrasound imaging at <https://huggingface.co/spaces/HReynaud/EchoFlow>.

Index Terms—Cardiac Ultrasound, Flow Matching, Foundation Model, Synthetic Dataset, Video Generation

I. INTRODUCTION

ADVANCEMENTS in artificial intelligence and deep learning have significantly benefited a variety of fields in healthcare, such as diagnosis, treatment planning, and patient care [38], [63]. Medical datasets are fundamental for these data-driven deep learning approaches, as they provide the critical information necessary for precise predictions and rigorous

analyses [36], [47]. However, the inherently sensitive nature of patient data, coupled with stringent privacy regulations and the challenges of obtaining consent, often limits the accessibility and dissemination of medical datasets.

Echocardiogram analysis exemplifies these challenges. Echocardiogram, or cardiac ultrasound, plays a pivotal role in assessing cardiac structure and function, as well as diagnosing cardiovascular diseases. Nevertheless, acquiring sufficient echocardiographic data is costly, as the acquisition process heavily depends on the sonographer’s expertise and it usually takes years to train qualified sonographers.

Recently, generative models such as Generative Adversarial Networks (GANs), Variational Auto-Encoders (VAEs) and diffusion models have emerged as powerful tools for producing high-quality images and videos in computer vision [5], [12], [19], [29], [39], [48], [51], [61]. Several recent works have successfully employed diffusion models to synthesise echocardiogram images [35], [56] and videos [10], [31], [44], [64]. They demonstrate good quality through commonly used quantitative metrics, however, few have evaluated the practical utility of synthetic data in clinical applications.

In this work, we introduce EchoFlow, a novel and systematic framework to synthesise echocardiogram videos. Clinical downstream tasks are utilised as a measurement to explicitly evaluate the practical utility of our synthetic data. Our framework consists of two main components: data generation and downstream evaluation. In the data generation stage, we first train an Adversarial Variational Auto-Encoder (A-VAE) for image reconstruction, using its encoder to define a latent representation of real data and its decoder to generate images from this representation. We then develop latent flow matching within the A-VAE-defined latent space to train both the Latent Image Flow Matching (LIFM) and Latent Video Flow Matching (LVFM) models. To safeguard patient privacy and mitigate risks of data leakage, a rigorous de-identification protocol, implemented via a Re-Identification (ReId) module, is incorporated. Once these four modules are trained, synthetic echocardiogram datasets are generated by using the LIFM model to produce individual frames, the ReId module for privacy filtering, and the LVFM model to generate echocardiogram videos in the latent space, which are subsequently decoded by the A-VAE decoder. In the downstream evaluation stage, Left Ventricular Ejection Fraction (EF) regression is used as a clinical downstream task to validate the clinical utility of our synthetic dataset. Specifically, we compare the performance of EF regression models trained on our synthetic

Manuscript received x;

This work was supported by Ultromics Ltd., the UKRI Centre for Doctoral Training in Artificial Intelligence for Healthcare (EP / S023283/1) and HPC resources provided by the Erlangen National High Performance Computing Center (NHR@FAU) of the Friedrich-Alexander-Universität Erlangen-Nürnberg (FAU) under the NHR project b180dc. NHR and high-tech agenda Bavaria (HTA) funding is partly provided by federal and Bavarian state authorities. NHR@FAU hardware is partially funded by the German Research Foundation (DFG) - 440719683. Support was also received from the ERC project MIA-NORMAL 101083647 and DFG KA 5801/2-1, INST 90/1351-1, and 512819079.

H. Reynaud is with the UKRI CDT in AI for Healthcare and Department of Computing, Imperial College London, London, UK (e-mail:hadrien.reynaud19@imperial.ac.uk). Q. Meng is with the School of Computer Science, University of Birmingham, Birmingham, UK and Department of Computing, Imperial College London, London, UK. A. Gomez is with Ultromics Ltd. P. Leeson is with Ultromics Ltd. and University of Oxford. B. Kainz is with the Department of Computing, Imperial College London, London, UK and Friedrich-Alexander University Erlangen-Nürnberg, DE.* Equal supervision.

data against identical models trained on real datasets.

A preliminary version of this work was presented at the MICCAI 2024 conference [44], where a Latent Diffusion Model (LDM) was employed for echocardiogram generation. Although [44] yielded high-quality synthesised echocardiograms, a gap persisted between the performance of the synthetic data and that of real data in downstream EF regression tasks. In contrast, this work thoroughly validates a broad range of VAE techniques and generative models, leading to a comprehensive data generation pipeline that produces synthetic echocardiograms with performance closely matching that of real data in clinical applications. Moreover, our work establishes a foundational framework for medical data generation, offering valuable insights into creating synthetic data with genuine clinical utility.

Contributions: Our main contributions are:

- We introduce a systematic and foundational framework that leverages flow matching techniques for echocardiogram synthesis. We are the first to use latent flow matching for cardiac ultrasound generation.
- We develop and thoroughly validate a comprehensive data generation pipeline. By optimizing the architecture, scale, and training protocols for latent space learning as well as image and video synthesis, our proposed pipeline produces high-fidelity echocardiogram videos.
- We introduce clinically relevant downstream tasks to assess the practical utility of our synthetic datasets. Importantly, our work is the first to generate synthetic echocardiogram videos that can achieve performance parity with real data in these tasks.
- We perform an extensive experimental analysis across three publicly available datasets. Our evaluations include quantitative and qualitative assessments of synthetic echocardiograms and downstream EF regression performance. Additionally, we compare the proposed method with state-of-the-art echocardiogram generation methods and conduct a detailed ablation study of the data generation sampling process.

II. RELATED WORKS

A. Generative Models for Image Synthesis

Image synthesis in computer vision has gained significant attention in recent years. GANs [18] have been widely used for image synthesis, as they enable efficient sampling of high-resolution images with good perceptual quality [5]. However, GANs often suffer from mode collapse and unstable training [1]. VAEs [28] also support efficient image synthesis [12] but they usually tend to produce blurry results.

Recently, diffusion models have emerged as a leading approach for generation tasks [20], [45], [48]. They offer stable training and excellent scalability, achieving high sample quality and broad mode coverage [14], [48]. Despite these strengths, evaluating and optimizing diffusion models in pixel space results in slow inference speeds and high training costs. To address these issues, researchers have moved the denoising process into latent spaces. For example, [45] trains a diffusion model in the latent space of a powerful pre-trained A-VAE.

This approach paved the way for many subsequent works, including the large-scale implementations known as Stable Diffusion [52]–[54]. Many following works have fine-tuned the pre-trained Stable Diffusion weights for specific tasks [6], [29]. Compared to diffusion models [20], [45] recent flow matching approaches offer greater data and compute efficiency [16], [30], [33]. Flow matching redefines the forward process as a direct path between the data distribution and a standard normal distribution. This offers a more straightforward transition from noise to data.

B. Generative Models for Video Synthesis

For video generation, popular image synthesis models have been adapted, such as GANs and VAEs [39], [51]. Diffusion models have demonstrated reasonable performance on videos with low temporal and spatial resolutions [23]. They have also achieved high-definition quality for longer samples when, *e.g.*, conditioned on text inputs [22], [27], [51]. Although these methods exhibit outstanding modelling capabilities, they often suffer from excessive computational requirements. To improve tractability, recent work have explored LDMs [45] for video generation [3], [19]. VideoLDM [3] extends LDMs to high-resolution video generation by converting pre-trained image LDMs into video generators through the insertion of temporal layers. Latent Video Diffusion Model (LVDM) [19] proposes a hierarchical diffusion model that operates in the video latent space, enabling the generation of long video sequences through a secondary model. More recently, a few studies have begun exploring flow matching techniques for more efficient video generation [26].

C. Ultrasound Generation

In the field of ultrasound generation, research has followed two primary directions. Some works focus on physics-based simulators [25], [50]. Others focus on generating individual ultrasound images with generative models. GAN-based methods have been well studied for ultrasound image synthesis. These approaches typically condition their models on complementary imaging modalities such as MRI, CT [58], [60], or simulated images [17], [59]. More recent works take advantage of diffusion models to achieve stable and controllable ultrasound image generation [35], [56]. Lately, ultrasound video generation is becoming a popular research area [10], [31], [64]. [32] presents a motion-transfer-based method for pelvic ultrasound videos, while [42] introduces a causal model for echocardiogram video generation. [43] further develops a diffusion model-based method for synthesizing echocardiogram videos. Although this approach produces high-quality ultrasound videos, it requires extensive sampling times. More recently, [44] leveraged latent diffusion models for faster and more temporally consistent echocardiogram generation.

D. Privacy-preserving Generation

Generative model such as diffusion-based and flow-based models, have a tendency to memorize their training set [8], [11], which raises privacy concerns. Two approaches have

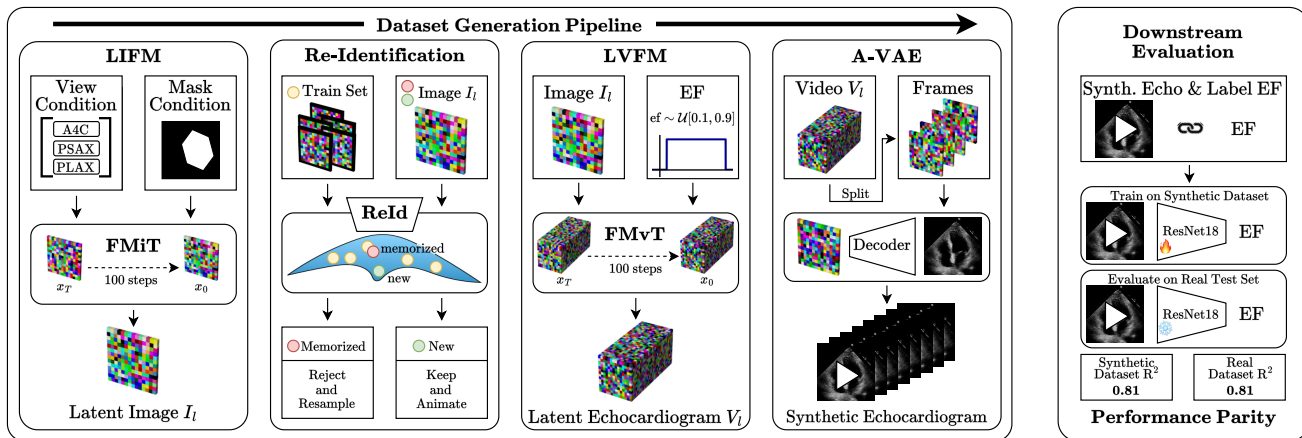


Fig. 1. Our EchoFlow framework. From left to right: The image generation model (LIFM), the privacy filter (Re-Identification), the video generation model (LVFM), the decoding stage (A-VAE) and our downstream evaluation. For each step, inputs are shown at the top, process in the middle and output at the bottom.

emerged to try and solve this problem, differential privacy [7], [15] and ReId [13]. For differential privacy, noise is added to the real samples during training, to prevent memorization. In ReId, generated samples are filtered during inference to detect any strong match between generated and real samples. Here, we focus on ReId, as it maintains model performance.

III. METHODS

The goal of this work is to achieve performance parity on downstream tasks between a model trained exclusively on synthetic data, and the same model trained on real data. In this section, we present the overarching framework we use to achieve this goal, as well as each individual component.

A. Framework

Our core components are (1) an A-VAE, used to define a domain-specific latent space, (2) a latent image generation model that can generate latent representation of cardiac ultrasound images, (3) a latent ReId model that can detect when a generated image is anatomically similar to an image from the training set and (4) a latent video generation model that can animate a latent cardiac ultrasound image into a latent video. The generated latent images and videos are decoded back to pixel space using the decoder of the A-VAE. By combining these four blocks, we enable the generation of synthetic datasets that retain the data quality of the real dataset on which the models were trained on, while preventing any real patient data leakage. We present our inference and evaluation pipeline in Figure 1.

At training time, it is essential to start by training the A-VAE (Section III-B), as it defines the latent space in which all other models will operate. The three other models are independent.

At inference time, we start by sampling a latent echocardiogram image, that acts as a candidate anatomy. This candidate anatomy is sent to our ReId model, which compares that anatomy with all existing training anatomies. If the similarity score is too high, the latent image is rejected and a new one is generated. Otherwise, the latent anatomy is used to condition

the latent video generation model, which animates the heart with a given EF score. This produces a sequence of frames, which are then decoded back into pixel space by using the A-VAE decoder.

B. Adversarial Variational Auto-Encoder

As training and sampling generative models at native resolution can be prohibitively expensive, we first compress the data into latent representation using A-VAEs [45]. This projects the input image to a 2D latent space. The 2D space allows the model to retain positional information effortlessly by maintaining the relative position of the image features.

Additionally to remedy blurry reconstruction problem, the decoder is shifted from a decoding task via Mean Squared Error (MSE) loss to a generation task with a strong prior, by introducing an adversarial objective in the loss formulation of the decoder. This loss forces the decoder to fill-in missing high frequency details that are lost during the encoding process, and thus not present in the latent space.

However, relying on a 2D latent space prevents the A-VAE from generating new samples from random noise, because the decoder network requires structured latent information, which cannot be obtained from simple numerical distributions. Additionally, the introduction of the adversarial loss makes the training less stable, as the decoder behaves like a GAN [1].

Existing general-purpose A-VAEs [2], [45], [54] can efficiently embed diverse images into a latent space, potentially removing the need for training a custom model. However, because they are trained on general image corpora, they lack the specialisation needed to fully capture echocardiography data, as shown in Table I. Therefore, we train our own A-VAEs from scratch, following best practices [2], [45].

The A-VAE forward pass is as follows. An encoder network $E_{\psi}(\cdot)$ maps an input image x_i to a latent space distribution, by predicting both the mean μ_i and the variance σ_i for that image. The latent variable z_i is sampled using the reparameterization trick (eq. (2)). z_i is then be decoded back to the image space

using a decoder network $D_\phi(\cdot)$. Formally,

$$\mu_i, \sigma_i = E_\psi(x_i), \quad (1)$$

$$z_i = \mu_i + \sigma_i \odot \epsilon_i, \quad \epsilon_i \sim \mathcal{N}(0, x_i), \quad (2)$$

$$\hat{x}_i = D_\phi(z_i). \quad (3)$$

We train $E_\psi(\cdot)$ and $D_\phi(\cdot)$ end-to-end through a reconstruction loss, an adversarial loss and a KL-divergence regularization term. The individual loss terms are given by:

$$\mathcal{L}_{\text{rec}} = \frac{1}{N} \sum_{i=1}^N \|x_i - \hat{x}_i\|^2, \quad (4)$$

$$\mathcal{L}_{\text{adv}} = -\mathbb{E}_{z \sim q_\theta(z|x)} [\log A(D_\phi(z))], \quad (5)$$

$$\mathcal{L}_{\text{KL}} = \frac{1}{2} \sum_{j=1}^J (1 + \log(\sigma_j^2) - \mu_j^2 - \sigma_j^2), \quad (6)$$

$$\mathcal{L}_{\text{VAE}} = \mathcal{L}_{\text{rec}} + \lambda \cdot \mathcal{L}_{\text{adv}} + \gamma \cdot \mathcal{L}_{\text{KL}}. \quad (7)$$

Here, \mathcal{L}_{rec} is the reconstruction loss computed using an MSE between the input image x_i and the reconstructed image \hat{x}_i . N is the number of samples in the batch. \mathcal{L}_{adv} is the adversarial loss, where the discriminator $A(\cdot)$ is a neural network trained end-to-end with the A-VAE, which assesses the quality of the generated image $D_\phi(z)$, and $q_\theta(z|x)$ is the encoder's output distribution. \mathcal{L}_{KL} is the KL-divergence regularization term over the latent space z , and J is the latent space dimension. λ and γ are hyperparameters used to adjust the weight of each term over the final loss.

Normalisation. While the KL regularization term forces the latent space distribution to resemble a Gaussian distribution, the resulting latent space is often skewed from such distribution due the precedence of reconstruction quality, expressed by a low value of γ in Equation (7). Nonetheless, having a Gaussian distributed latent space is desirable for generative models, as they are easier to train over Gaussian distributed data. As such, during inference, we normalise any sampled latent z_i channel-wise, based on statistics computed over the corresponding latent training set. Formally,

$$\mu_k = \frac{1}{N} \sum_{i=1}^N [z_i]_k, \quad \text{for } k = 1, \dots, K, \quad (8)$$

$$\sigma_k = \sqrt{\frac{1}{N} \sum_{i=1}^N ([z_i]_k - \mu_k)^2}, \quad \text{for } k = 1, \dots, K, \quad (9)$$

$$[\hat{z}_i]_k = \frac{[z_i]_k - \mu_k}{\sigma_k}, \quad \text{for } k = 1, \dots, K \quad (10)$$

where $[z_i]_k$ denotes the k^{th} channel of the latent code z_i , and the operations in Equation (10) are applied channel-wise.

C. Latent Flow Matching Models

Flow matching is a deterministic framework that learns a continuous mapping from a simple distribution to the target data by approximating a velocity field. Rather than relying on a stochastic reverse process like diffusion models, flow matching trains a neural network to follow a well defined interpolation path between noise and data.

Let p_{data} denote the data distribution and p_{prior} a simple distribution (e.g. Gaussian). We define a family of intermediate distributions $\{p_t(\mathbf{x})\}_{t \in [0,1]}$ such that $p_0 = p_{\text{data}}$ and $p_1 = p_{\text{prior}}$. We use linear interpolation

$$\mathbf{x}_t = (1-t)\mathbf{x}_0 + t\mathbf{x}_1, \quad (11)$$

with $\mathbf{x}_0 \sim p_{\text{data}}$ and $\mathbf{x}_1 \sim p_{\text{prior}}$. The corresponding ground-truth velocity along the path is given by

$$u(\mathbf{x}_0, \mathbf{x}_1) = \frac{d\mathbf{x}_t}{dt} = \mathbf{x}_1 - \mathbf{x}_0, \quad (12)$$

where $u(\mathbf{x}_0, \mathbf{x}_1)$ represents the instantaneous velocity vector that drives the interpolation from the data point \mathbf{x}_0 to the noise sample \mathbf{x}_1 .

Training involves learning a time-dependent vector field $v_\theta(\mathbf{x}, t)$ by minimizing the regression loss:

$$\mathcal{L}_{\text{FM}} = \mathbb{E}_{t, \mathbf{x}_0, \mathbf{x}_1} [\|v_\theta(\mathbf{x}_t, t) - (\mathbf{x}_1 - \mathbf{x}_0)\|^2]. \quad (13)$$

Once trained, new data samples are generated by drawing a sample $\mathbf{x}_1 \sim p_{\text{prior}}$. We then discretize the time interval $[0, 1]$ into N equal steps with $\Delta t = 1/N$ and apply the Euler ODE sampler to integrate the ODE

$$\frac{d\mathbf{x}}{dt} = v_\theta(\mathbf{x}, t), \quad (14)$$

backwards from $t = 1$ to $t = 0$. At each discrete time step, the sample is updated as

$$\mathbf{x}_{t-\Delta t} = \mathbf{x}_t - \Delta t \cdot v_\theta(\mathbf{x}_t, t). \quad (15)$$

After N steps, the final state \mathbf{x}_0 is obtained, which approximates the target data distribution.

Flow Matching is compatible with any backbone architecture. In this work, we focus on UNet [20], [46] and Transformers [37], [62]. We propose a Spatial-only model, and a Spatio-Temporal model. Our UNet architecture relies on Attention-based ResNet blocks [49]. For the Spatio-Temporal UNet, we interleave Spatial and Temporal ResNet blocks and Spatial and Temporal Attention blocks.

Our Transformer-based architecture follows the implementation from [37]. We transform the input image or video into a sequence of patches and add positional (and temporal) embeddings to each patch. The resulting patches are then sent through a sequence of transformer blocks. The output is projected and reshaped back into an image (or video) with the same dimension as the input. For the video, we use Spatio-Temporal transformer blocks which alternate Spatial and Temporal Attention.

Conditioning. We define two sets of conditionings, one for the image models and one for the video models. The LIFM models are conditioned on a segmentation mask and a class index corresponding to the desired view (Apical 4 Chamber (A4C), Parasternal Short Axis (PSAX) or Parasternal Long Axis (PLAX)). This allows us to control the view but also the area covered by the left ventricle. The LVFM models are conditioned on an anatomy (i.e., an echocardiogram frame) and an EF score, shifting the task from pure generation to frame-animation. We ensure during training that none of the generated frames are identical to the conditioning frame, to

force the model to disentangle anatomy understanding from the generation task.

To improve the adherence of the generated samples to our conditionings, we rely on Classifier-Free Guidance (CFG) [21]. The models are trained with a given probability to drop some or all their conditionings, which allows us to sample both a conditional sample and an unconditional sample during inference, and apply CFG such that

$$v_{unc} = v_{\theta}(\mathbf{x}_t, t), \quad v_{cond} = v_{\theta}(\mathbf{x}_t, t, c_1, c_2), \quad (16)$$

$$v_{cfg} = v_{unc} - \lambda_{cfg} \cdot (v_{cond} - v_{unc}) \quad (17)$$

$$\mathbf{x}_{t-\Delta t} = \mathbf{x}_t - \Delta t \cdot v_{cfg}, \quad (18)$$

where c_1, c_2 are conditionings (*e.g.*, an EF score and an anatomy), and λ_{cfg} is the CFG scale. If $\lambda_{cfg} = 0$, the sampling is unconditioned, while setting $\lambda_{cfg} = 1$ ignores CFG.

D. Re-Identification

ReId is applied as a filter on generated samples, and does not directly interact with any of the generative models. This is extremely powerful as it does not compromise the generative model performance, while still enforcing privacy. Nonetheless, it also means that only the filtered data is privacy compliant, not the generative models themselves. For the objective of this work, this is a suitable solution.

Our ReId models operate over the latent space, which avoids the expensive operation of projecting latent images back to pixel space, and makes training and inference computationally efficient. We train ReId with a contrastive learning approach. The objective is to learn an encoder $\text{Enc}(\cdot)$ that projects an input image I into a 1D latent space l , capturing its anatomy.

At each training step, two videos V_a and V_b are selected. From V_a , two random frames I_{a_1} and I_{a_2} are sampled, while from V_b a single frame I_b is sampled. The frames are then paired to define $\text{pair}_{\text{pos}} = \{I_{a_1}, I_{a_2}\}$ and $\text{pair}_{\text{neg}} = \{I_{a_1}, I_b\}$. The encoder projects each image into the latent space $l = \text{Enc}(I)$. The training objective is to ensure that the latent representations of the positive pair, $l_{a_1} = \text{Enc}(I_{a_1})$ and $l_{a_2} = \text{Enc}(I_{a_2})$, are close, while the representation of the negative pair, l_{a_1} and $l_b = \text{Enc}(I_b)$, are pushed apart. This is achieved by optimizing a contrastive loss function. Formally, we define the sigmoid function $\mathcal{S}(x) = \frac{1}{1+e^{-x}}$, and the training procedure

$$\hat{l}_{a_1} = \mathcal{S}(l_{a_1}), \quad \hat{l}_{a_2} = \mathcal{S}(l_{a_2}), \quad \hat{l}_b = \mathcal{S}(l_b), \quad (19)$$

$$\Delta_{\text{pos}} = \left| \hat{z}_{a_1} - \hat{l}_{a_2} \right|, \quad \Delta_{\text{neg}} = \left| \hat{l}_{a_1} - \hat{l}_b \right|, \quad (20)$$

$$\hat{y}_{\text{pos}} = W \Delta_{\text{pos}} + b, \quad \hat{y}_{\text{neg}} = W \Delta_{\text{neg}} + b, \quad (21)$$

$$\mathcal{L}_{\text{reid}} = \text{BCE}(\hat{y}_{\text{pos}}, 1) + \text{BCE}(\hat{y}_{\text{neg}}, 0). \quad (22)$$

Here, W and b are learnable parameters trained end-to-end with $\text{Enc}(\cdot)$ and ‘BCE’ is the Binary Cross-Entropy loss.

During inference, the trained ReId encoder $\text{Enc}(\cdot)$ is applied to an input image I to obtain an anatomical representation. Since the training set comprises videos and all frames within a video have very similar anatomical embeddings, only the first encoded frame $l_v^1 = \text{Enc}(I_v^1)$ from each video v is used to represent a whole video.

To determine the similarity between the input image and the training set, the Pearson correlation coefficient is computed between the latent representation l of the input and all training representation l_v^1 :

$$\rho(l, l_v^1) = \frac{\text{cov}(l, l_v^1)}{\sqrt{\text{var}(l) \text{var}(l_v^1)}}. \quad (23)$$

The maximum correlation value across all training videos is then selected:

$$\rho_{\text{max}} = \max_v \rho(l, l_v^1). \quad (24)$$

Finally, this maximum similarity score ρ_{max} is compared against a precomputed privacy threshold τ . If $\rho_{\text{max}} \geq \tau$, the input image is considered too similar to the training data, and flagged as not respecting privacy guarantees. The privacy threshold τ is determined by comparing the similarities between the real training and real validation sets. Let $\{l_i^{1, \text{val}}\}$ denote the embeddings from the validation set first frames. The Pearson correlation coefficient is computed between each training embedding and every validation embedding, forming a correlation matrix C . For each training sample v , the maximum correlation value is extracted:

$$\rho_v^{\text{max}} = \max_i \rho(l_v^1, l_i^{1, \text{val}}). \quad (25)$$

The threshold τ is then set as the p^{th} percentile of these maximum correlations:

$$\tau = \text{percentile}\left(\{\rho_v^{\text{max}} : v \in \text{training set}\}, p\right), \quad (26)$$

where p is a predefined cutoff percentage set to 95%. This approach ensures that τ reflects the inherent similarity between training and validation samples, providing a reliable benchmark for assessing anatomical similarity.

E. Ejection Fraction Regression

We use downstream task performance as the main metric for this work, as we believe it is the best way to demonstrate the quality of a synthetic dataset. In the context of echocardiograms, EF regression is the most common task [36], [41]. The goal of EF regression is to estimate a continuous scalar value from a sequence of input frames. The EF regression task is performed on datasets of the form $\mathcal{D}_{ef} = \{(V, y)\}$ that consist of a list of pairs of video V and their corresponding ground-truth EF score y . During training, a video V is fed into a regression model $\text{Reg}(\cdot)$ to obtain an estimate $\hat{y} = \text{Reg}(V)$. The model is optimised by minimizing the MSE loss between the true EF score y and the estimated EF score \hat{y} such that $\mathcal{L}_{\text{reg}} = (y - \hat{y})^2$. This loss encourages the regression model to accurately capture the cardiac features present in the video, leading to reliable predictions of the EF.

IV. EXPERIMENTS

A. Experimental setups

1) *Data*: To facilitate reproducibility, we rely exclusively on public echocardiogram datasets EchoNet-Dynamic (Dynamic) [36], EchoNet-Pediatric (Pediatric) [40] and EchoNet-LVH (LVH) [55], as real datasets. Dynamic contains exclusively A4C views, and we adopt its original training, validation, and testing split. Pediatric contains both A4C and PSAX

views, so we split it into two separate datasets Pediatric (A4C) and Pediatric (PSAX). Both Pediatric datasets are originally split into 10 folds, and we arbitrarily use the first 8 folds for training, the 9th for validation and the 10th for testing. LVH contains exclusively PLAX views, and we use its original splits. Every echocardiogram in the Dynamic and Pediatric datasets comes with an expert-labelled EF score and two segmented frames, corresponding to an End-Systolic (ES) and End-Diastolic (ED) key frame. The LVH dataset comes with tracings of the left ventricle. We use these tracings to estimate the ES and ED volumes (ESV and EDV) through the Teichholz formula [57]. This allows us to calculate an approximate EF score as $EF = \frac{EDV - ESV}{EDV} \times 100$. Our image generation models take a segmentation mask as a condition. To allow each frame of Dynamic and Pediatric to have a paired segmentation, we train a DeepLabV3 segmentation model [9], and use it to segment every unlabelled frame. We use empty masks for LVH as it does not have segmentation labels. The size of each dataset and each split is reported in Table VII. We also rely on TMED2 [24] for A-VAE experiments. For TMED2, we disregard any split and labels and build a large database of ultrasound images by merging all available images.

2) Evaluation metrics: To evaluate the performance of A-VAEs, we compute both reconstruction metrics and generative metrics. Reconstruction metrics are evaluated pair-wise between an original image and its reconstructions. Generative metrics are computed dataset-wise between the real datasets and the reconstructed datasets. For the LIFM and the LVFM, we assess the image generation quality using Fréchet Inception Distance (FID) and Inception Score (IS) and video generation quality using Fréchet Video Distance (FVD). We also measure model efficiency in terms of number of parameters, Floating-point Operations per Second (FLOPs) and inference time. Beyond these metrics, we use a clinical downstream task as a measurement to ensure that synthetic datasets can effectively support medical imaging research and clinical translation. Specifically, we train individual EF regression models on every real dataset and its exclusively synthetic counterpart, and systematically assess performance on the real test datasets. We use the Coefficient of Determination (R^2), Mean Absolute Error (MAE) and Root mean square error (RMSE) metrics to assess the precision of the EF regression models.

B. Adversarial Variational Auto-Encoders

1) Data preparation: The A-VAEs training needs a large collection of images. To build it, we sample 1 in 5 frames from every echocardiogram video in our datasets' training split. Then, to increase robustness and generalization capabilities, we use the TMED2 [24] echocardiogram collection on top of our existing video datasets. This combination leads to a total of 1 312 623 training frames, all with resolution $112 \times 112 \times 3$.

2) Hyperparameters: All our A-VAEs rely on an encoder-decoder architecture, based on a succession of convolutional ResNet and downsampling blocks. We train three variants, where we vary the depth of the encoder and decoder which impacts the spatial compression factor, as well as the number of latent space channels. We define (1) A-VAE-4f8, with 4

latent channels and a spatial compression factor of 8, resulting in a latent space of $14 \times 14 \times 4$, (2) A-VAE-4f4, with 4 channels, compression $4\times$, and a $28 \times 28 \times 4$ latent space, and (3) A-VAE-16f8, with 16 channels, compression $8\times$, and a $14 \times 14 \times 16$ latent space. Our models cover three latent space resolutions, which is the main factor we want to evaluate.

3) Training: Our A-VAEs are trained for 10.5 days on $8 \times A40$ GPUs, resulting in 2000 GPU-hours per A-VAE, and 300 epochs for each. The batch size is fixed to 32 per GPU, with a gradient accumulation of 2, resulting in a total batch size of 512. The learning rate is set to $1e-3$ and the adversarial loss starts after 30 epochs of training, in order to let the model learn from the reconstruction loss first.

4) Baselines: We compare the performance of our A-VAEs with four general A-VAEs [2], [45], [52], [54] and one echocardiogram-specific A-VAE [44] and report the results in Table I. All the general A-VAEs are trained on general image dataset. SD 1.4 A-VAE [45] is the first widely used A-VAE, and SD 2.1 A-VAE [52] and SD 3.5 A-VAE [54] are its successors, which rely on very similar architectures and data mix. FLUX.1 A-VAE [2] is a recent state-of-the-art general A-VAE that excels at image reconstruction. EchoSyn A-VAE [44] is trained exclusively on an echocardiogram-specific data mix.

5) Evaluation: We compare the performance all the A-VAEs by reconstructing the entire real datasets and evaluating both reconstructions and generative metrics. Results are presented in Table I, where we show all the metrics for Dynamic and only our selected models metrics for Pediatric and LVH.

We observe that the FLUX.1 A-VAE is the best performing off-the-shelf model, mostly due to its larger latent space dimension that relies on 16 channels instead of 4. Our own models follow a similar trend, where the A-VAE-16f8 model performs substantially better than the A-VAE-4f8 model. With the A-VAE-4f4 model, we maintain the same total compression factor as with the A-VAE-16f8, but trade the number of channels for a higher spatial resolution. This results in our best performing model, where more of the spatial information is retained. Our A-VAE-4f4 and A-VAE-16f8 models are by far the best on reconstruction metrics, but perform on-par with FLUX.1 [2] when it comes to generative metrics.

To further our comparison between our best A-VAEs and FLUX.1 [2], we compute the joint differential entropy of each model's latent space. We find that on our medical task, FLUX.1 achieves 164 nats, while A-VAE-4f4 achieves 1456 nats and A-VAE-16f8 reaches 1695 nats. The nats number measures the information entropy (or uncertainty) contained in a set. A higher nats mean that the model covers a larger data range in the latent space. These numbers show that the echocardiogram images in the FLUX.1 latent space are all encoded over a very small area of the latent space, while in the A-VAE-4f4 and A-VAE-16f8 models, the echocardiograms cover a much larger space. This is to be expected, as FLUX.1 A-VAE was trained on a larger diversity of images, and thus groups similar-looking images in a fraction of the space. This also mean that training a generative model on the FLUX.1 latent space constrains the model to a small subspace. This is not desirable and justifies using custom A-VAEs when working on domain-specific data. Therefore, for later experiments, we

TABLE I
PERFORMANCE OF THE VAE. BEST VALUES ARE IN BOLD, SECOND BEST ARE UNDERLINED.

Dynamic (A4C)	Latent Res.	Reconstruction Metrics					Generative Metrics		
		MSE↓	MAE↓	SSIM↑	PSNR (dB)↑	LPIPS↓	FID↓	FVD ₁₆ ↓	IS↑
SD 1.4 A-VAE [45]	14 × 14 × 4	0.0051±0.0011	0.0366±0.0056	0.7290±0.0457	22.99±1.02	0.1169±0.0113	39.31	141.76	2.52±0.10
SD 2.1 A-VAE [52]	14 × 14 × 4	0.0043±0.0009	0.0340±0.0050	0.7597±0.0418	23.72±0.95	0.1021±0.0099	30.04	174.22	<u>2.54</u> ±0.09
SD 3.5 A-VAE [54]	14 × 14 × 16	0.0028±0.0006	0.0280±0.0046	0.8272±0.0340	25.62±1.09	0.0900±0.0075	33.61	<u>89.41</u>	2.53±0.10
FLUX.1 A-VAE [2]	14 × 14 × 16	0.0017±0.0004	0.0216±0.0038	0.8928±0.0276	27.87±1.21	0.0409±0.0060	5.19	95.78	2.56 ±0.07
EchoSyn A-VAE [44]	14 × 14 × 4	0.0034±0.0008	0.0305±0.0050	0.7999±0.0444	24.79±1.08	0.0750±0.0101	12.55	90.16	2.37±0.07
A-VAE 4f8 (ours)	14 × 14 × 4	0.0034±0.0008	0.0301±0.0050	0.7996±0.0442	24.87±1.14	0.0787±0.0101	13.76	119.22	2.37±0.08
A-VAE 4f4 (ours)	28 × 28 × 4	0.0010 ±0.0003	0.0170 ±0.0034	0.9244 ±0.0240	30.26 ±1.42	<u>0.0346</u> ±0.0065	3.62	61.86	2.48±0.07
A-VAE 16f8 (ours)	14 × 14 × 16	<u>0.0010</u> ±0.0003	<u>0.0175</u> ±0.0036	<u>0.9173</u> ±0.0264	<u>30.09</u> ±1.45	0.0345 ±0.0070	<u>4.10</u>	104.94	2.46±0.07
Pediatric (A4C)	Latent Res.	MSE↓	MAE↓	SSIM↑	PSNR (dB)↑	LPIPS↓	FID↓	FVD ₁₆ ↓	IS↑
A-VAE 4f4 (ours)	28 × 28 × 4	0.0003 ±0.0002	0.0090 ±0.0030	0.9690 ±0.0133	35.79 ±2.23	0.0266 ±0.0086	1.81	<u>6.00</u>	2.93±0.00
A-VAE 16f8 (ours)	14 × 14 × 16	<u>0.0003</u> ±0.0002	<u>0.0097</u> ±0.0035	<u>0.9570</u> ±0.0217	<u>35.59</u> ±2.44	<u>0.0293</u> ±0.0115	<u>1.69</u>	7.94	2.96±0.00
Pediatric (PSAX)	Latent Res.	MSE↓	MAE↓	SSIM↑	PSNR (dB)↑	LPIPS↓	FID↓	FVD ₁₆ ↓	IS↑
A-VAE 4f4 (ours)	28 × 28 × 4	0.0003 ±0.0002	0.0095 ±0.0033	0.9680 ±0.0146	35.50 ±2.38	0.0274 ±0.0094	1.86	<u>5.39</u>	3.24±0.12
A-VAE 16f8 (ours)	14 × 14 × 16	<u>0.0004</u> ±0.0002	<u>0.0102</u> ±0.0039	<u>0.9570</u> ±0.0225	<u>35.27</u> ±2.60	<u>0.0297</u> ±0.0122	1.51	7.37	3.20±0.12
LVH (PLAX)	Latent Res.	MSE↓	MAE↓	SSIM↑	PSNR (dB)↑	LPIPS↓	FID↓	FVD ₁₆ ↓	IS↑
A-VAE 4f4 (ours)	28 × 28 × 4	0.0010 ±0.0003	0.0170 ±0.0032	0.9308 ±0.0203	30.31 ±1.29	<u>0.0352</u> ±0.0059	<u>4.58</u>	26.22	2.62±0.11
A-VAE 16f8 (ours)	14 × 14 × 16	<u>0.0010</u> ±0.0003	<u>0.0175</u> ±0.0033	<u>0.9234</u> ±0.0228	<u>30.15</u> ±1.33	0.0351 ±0.0064	4.09	30.08	2.56±0.10

only consider our A-VAE-4f4 and A-VAE-16f8 models.

C. Latent Image Flow Matching Models

1) *Data preparation*: The LIFM models are trained on latent spaces. We pre-encode all the training videos with the A-VAE-4f4 and A-VAE-16f8 models, resulting in two latent datasets per real dataset. Additionally, instead of saving the latent space z (see eq. (2)), we save the outputs of the encoder μ and σ (see eq. (1)). This allows us to sample from the latent representation of each image during training, thus increasing the diversity and robustness of our generative models.

2) *Hyperparameters*: We train 15 different LIFM models, where we vary four hyperparameters, (1) UNet [20] and Transformer (Flow Matching Image Transformer (FMiT)) [37] backbone architectures, (2) $28 \times 28 \times 4$ and $14 \times 14 \times 16$ latent space dimensions, (3) Small, Base and Large model sizes, (4) patch size 2 or 4 for the FMiT-4f4 model.

3) *Training*: The models are trained on $8 \times A40$ GPUs with for a total batch size of 1024. The models are trained for 1 000 000 steps with a learning rate of $5e-5$, BF16 precision, and the training time varies from 640 to 3 600 GPU-hours.

4) *Baselines*: We compare our image generation models with the Latent Image Diffusion Model (LIDM) from [44]. This model relies on diffusion to train and sample from the model, and uses a latent space with resolution $14 \times 14 \times 4$.

5) *Evaluation*: We report the metrics for the LIFM models and the LIDM [44] in Table II. All our models are sampled for 100 steps using the Euler ODE sampling method.

From these experiments, we observe that performance scales with the number of parameters of the models. Our UNet-S-16f8 outperforms the LIDM-4f8 [44], while having a similar architecture, parameter count and latent spatial resolution. This improvement comes from our improved A-VAEs, training hyperparameters and increased channel count. The increased spatial resolution of 4f4 models comes at a significant computational cost (FLOPs) and inference time. We can see that the UNet-L-4f4 and FMiT-L/2-4f4 perform similarly, with a slight edge for the UNet.

We find that a higher spatial latent resolution yields better performance, but increases computational cost, marking a clear trade-off between image quality and inference speed.

D. Latent Video Flow Matching Models

1) *Data preparation*: The LVFM models are trained on the same latent space with the same sampling strategy as the LIFM models. We sample a latent video and its corresponding EF score, and extract one random frame from the video sequence. Then, we extract a 2s sample from the video, and resample it to 64 frames. The EF score and the random frame acts as our input conditionings, while the 64-frame video acts as our target. 2s ensure that we cover at least one entire heartbeat.

2) *Hyperparameters*: We train 5 LVFM models, varying the same hyperparameters as in the LIFM experiments, but limited to the Small variants, due to computational constraints. We explore a Spatio-Temporal UNet (STUnet) [4] as well as a Spatio-Temporal Transformer (Flow Matching video Transformer (FMvT)) [34]. We also explore two latent space resolutions ($28 \times 28 \times 4$ and $14 \times 14 \times 16$), and the impact of the patch size over the FMvT-4f4 performance. Given the scaling laws observed over the LIFM model, larger LVFM models would perform better.

3) *Training*: LVFM models are expensive to train, as the additional temporal dimension acts as a batch size increase. The models are trained for 1 000 000 steps with a learning rate of $1e-4$ and a total batch size of 512. The number of GPUs depends on the model size and varies from 8 to 64 H100 GPUs. The total training time ranges from 1 500 to 20 000 GPU-hours.

4) *Baselines*: We compare with two other works that explored echocardiogram synthesis over the Dynamic datasets, namely EchoDiffusion [43] and EchoSyn [44] (LVDM-4f8). We note that EchoDiffusion is a pixel-space diffusion model, and LVDM-4f8 is a latent diffusion model.

5) *Evaluation*: We present the metrics in Table III. The models are sampled for 100 steps with an Euler ODE sampler.

TABLE II
PERFORMANCE OF THE IMAGE GENERATION MODELS.

Model	Latent Res.	Param.	FLOPs	Inference	Dynamic (A4C)		Pediatric (A4C)		Pediatric (PSAX)		LVH (PLAX)	
					FID↓	IS↑	FID↓	IS↑	FID↓	IS↑	FID↓	IS↑
LIDM-4f8 [44]	14 × 14 × 4	74 M	–	–	17.3	2.42±0.02	13.7	2.86±0.03	16.8	3.05±0.03	–	–
UNet-S-16f8	14 × 14 × 16	50 M	1.30 G	37.0 ms	13.35	2.49±0.01	28.52	2.93±0.01	16.75	2.76±0.02	22.41	2.26±0.02
UNet-B-16f8	14 × 14 × 16	140 M	4.22 G	38.1 ms	8.89	2.54±0.02	22.54	3.03±0.02	10.21	2.93±0.02	16.76	2.37±0.01
UNet-L-16f8	14 × 14 × 16	560 M	14.33 G	57.3 ms	8.79	2.56±0.02	24.05	3.05±0.03	9.87	2.92±0.03	16.21	2.34±0.01
UNet-S-4f4	28 × 28 × 4	50 M	5.16 G	48.8 ms	7.47	2.53±0.02	9.51	3.01±0.03	6.70	3.04±0.02	14.10	2.43±0.02
UNet-B-4f4	28 × 28 × 4	140 M	14.31 G	79.6 ms	5.02	2.55±0.02	6.63	3.02±0.02	6.24	3.05±0.03	11.66	2.48±0.02
UNet-L-4f4	28 × 28 × 4	560 M	57.16 G	173.1 ms	4.47	2.58±0.01	6.22	3.06±0.01	6.15	3.14±0.03	11.19	2.45±0.01
FMiT-S/2-16f8	14 × 14 × 16	36 M	1.06 G	21.9 ms	11.11	2.49±0.02	33.19	2.87±0.02	17.91	2.77±0.02	11.99	2.34±0.02
FMiT-B/2-16f8	14 × 14 × 16	146 M	4.22 G	23.4 ms	10.08	2.50±0.02	31.19	2.94±0.02	14.35	2.78±0.03	11.33	2.34±0.01
FMiT-L/2-16f8	14 × 14 × 16	512 M	15.0 G	39.6 ms	9.69	2.47±0.02	23.62	3.04±0.02	10.90	2.97±0.02	11.36	2.33±0.02
FMiT-S/4-4f4	28 × 28 × 4	36 M	1.06 G	23.3 ms	12.43	2.48±0.03	22.84	2.88±0.02	17.43	2.82±0.01	13.43	2.44±0.02
FMiT-B/4-4f4	28 × 28 × 4	146 M	4.22 G	20.8 ms	11.34	2.50±0.02	15.63	2.94±0.02	13.11	2.87±0.02	12.15	2.46±0.02
FMiT-L/4-4f4	28 × 28 × 4	512 M	15.0 G	51.0 ms	8.52	2.54±0.02	9.95	2.98±0.03	8.12	3.05±0.02	11.46	2.46±0.02
FMiT-S/2-4f4	28 × 28 × 4	36 M	4.19 G	22.5 ms	8.09	2.52±0.02	16.02	2.95±0.02	9.10	3.00±0.02	7.65	2.51±0.02
FMiT-B/2-4f4	28 × 28 × 4	146 M	16.72 G	46.3 ms	7.50	2.52±0.02	12.88	2.97±0.02	7.51	3.02±0.03	7.41	2.51±0.01
FMiT-L/2-4f4	28 × 28 × 4	512 M	59.42 G	135.3 ms	6.79	2.53±0.03	8.18	3.01±0.02	5.78	3.07±0.02	6.76	2.51±0.01

TABLE III
PERFORMANCE COMPARISON OF THE VIDEO GENERATION MODELS

Model	Latent Res.	Params.	FLOPs	Inference	Dynamic (A4C)			Pediatric (A4C)			Pediatric (PSAX)			LVH (PLAX)		
					FID↓	FVD ₁₆ ↓	IS↑	FID↓	FVD ₁₆ ↓	IS↑	FID↓	FVD ₁₆ ↓	IS↑	FID↓	FVD ₁₆ ↓	IS↑
EchoDiffusion [43]	64 × 112 × 112	95 M	–	279.00 s	24.0	228	2.59±0.06	–	–	–	–	–	–	–	–	–
LVDM-4f8 [44]	64 × 14 × 14 × 4	144 M	–	2.40 s	17.4	71.4	2.31±0.08	24.8	112.2	2.69±0.18	33.0	126.9	2.49±0.09	–	–	–
STUNet-S-16f8	64 × 14 × 14 × 16	46 M	79.86 G	1.92 s	23.81	173.0	2.21±0.05	36.47	317.0	2.50±0.07	57.36	379.4	2.49±0.08	30.80	215.6	2.23±0.06
STUNet-S-4f4	64 × 28 × 28 × 4	46 M	317.19 G	4.80 s	13.73	40.0	2.40±0.06	19.44	107.6	2.78±0.12	26.38	135.3	2.87±0.09	14.14	49.4	2.53±0.10
FMvT-S/2-16f8	64 × 14 × 14 × 16	36 M	103.51 G	0.71 s	13.83	85.9	2.36±0.04	21.69	195.5	2.71±0.11	34.62	218.2	2.72±0.11	15.33	74.5	2.43±0.07
FMvT-S/4-4f4	64 × 28 × 28 × 4	36 M	103.51 G	0.74 s	14.78	48.8	2.38±0.05	21.05	153.8	2.80±0.13	31.64	181.2	2.78±0.08	14.80	46.9	2.50±0.09
FMvT-S/2-4f4	64 × 28 × 28 × 4	36 M	430.31 G	2.94 s	7.92	28.1	2.46±0.06	12.26	75.4	2.88±0.14	16.77	84.6	2.99±0.09	7.71	23.2	2.58±0.06

Based on the results in Table III, we see that FMvT outperforms the STUNet [4]. We believe that this is due to the higher performance of the temporal attention modules and increased stability of FMvT, observed during training. Despite all models having a similar parameter count, FMvT-S/2-4f4 beats all other model by a significant margin. It is also the most computationally expensive model, because it operates on a higher resolution latent space. By picking a better latent space dimension and training the model longer, FMvT-S/2-4f4 beats all previous state-of-the-art models while being 2–3× smaller. When sampling the FMvT-S/2-4f4 model we reach optimal performance when using 100 steps, according to Table IV, while keeping the sampling time similar to the previous state-of-the-art model [44]. Based on these results, we select FMvT-S/2-4f4 as our main video generation model for all further experiments. We visually compare models in Figure 2.

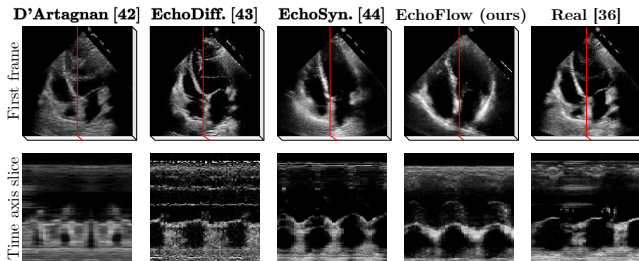


Fig. 2. Qualitative comparison of recent echocardiogram synthesis methods in spatial and temporal domain.

6) *Sampling Parameters*: We evaluate the impact of sampling steps over the FMvT-S/2-4f4 performance in Table IV.

We observe that the results with 25 sampling steps outperform the previous state-of-the-art [44], but we hit the point of diminishing returns at 100 sampling steps. Therefore, we use a 100 sampling steps.

We also explore the impact of CFG over the FMvT-S/2-4f4 model performance in Table VI. The first row, where $\lambda_{\text{cfg}} = 0$, shows the performance of the unconditioned or partially conditioned model. Indeed, v_{unc} in eq. (16) can be fully unconditional, or partially conditioned if we pass either the EF or the anatomical frame to the model. By selectively passing none or one of these conditions, we orient the CFG process in different directions. Therefore, for experiments with $\lambda_{\text{cfg}} = 0$, we see that the model performance heavily depends on the input anatomy, as removing the anatomy (rows 0 and 2), significantly degrades performance. When removing only the EF input (row 1), the visual performance does not degrade.

The $\lambda_{\text{cfg}} = 1$ row shows the baseline model, where CFG is not applied. There is no consensus on which value to set for λ_{cfg} . Nonetheless, $\lambda_{\text{cfg}} = 1$ maximises none of the metrics. The other consideration is that a higher λ_{cfg} decreases sample diversity [21]. Therefore, we select $\lambda_{\text{cfg}} = 2$ with no negative conditionings (\emptyset). This configuration demonstrates increased overall performance on most metrics.

E. Re-Identification Models

1) *Data preparation*: To train the ReID models, we use the real latent datasets, encoded with A-VAE-4f4. We follow the method described in section III-D for sampling.

2) *Hyperparameters*: We use a ResNet18 model, which takes as input a single latent image with resolution $28 \times 28 \times 4$

TABLE IV
VIDEO GENERATION PERFORMANCE PER SAMPLING STEPS.

Steps	Inference	Dynamic (A4C)			Pediatric (A4C)			Pediatric (PSAX)			LVH (PLAX)		
		FID \downarrow	FVD \downarrow	IS \uparrow	FID \downarrow	FVD \downarrow	IS \uparrow	FID \downarrow	FVD \downarrow	IS \uparrow	FID \downarrow	FVD \downarrow	IS \uparrow
5	0.26s	56.62	374.3	2.13 \pm 0.05	39.01	394.0	2.61 \pm 0.12	46.50	496.3	2.83 \pm 0.11	61.02	523.5	2.26 \pm 0.09
10	0.60s	24.24	126.6	2.32 \pm 0.05	19.64	158.5	2.77 \pm 0.15	23.76	164.2	3.02 \pm 0.09	26.77	172.5	2.39 \pm 0.09
25	1.00s	11.06	42.2	2.40 \pm 0.07	13.18	77.8	2.85 \pm 0.14	16.73	82.6	3.02 \pm 0.10	11.72	46.9	2.52 \pm 0.06
50	1.64s	8.73	30.7	2.43 \pm 0.05	12.09	70.6	2.91 \pm 0.16	15.98	81.3	3.03 \pm 0.06	8.94	26.1	2.56 \pm 0.08
100	2.94s	7.92	28.1	2.46 \pm 0.06	12.26	75.4	2.88 \pm 0.14	16.77	84.6	2.99 \pm 0.09	7.71	23.2	2.58 \pm 0.06
200	5.61s	7.27	28.0	2.48 \pm 0.05	12.28	78.3	2.91 \pm 0.16	16.90	90.6	3.03 \pm 0.10	7.63	23.4	2.58 \pm 0.08
500	13.71s	7.44	29.1	2.47 \pm 0.07	11.90	79.2	2.87 \pm 0.12	16.59	92.5	3.03 \pm 0.09	7.31	24.6	2.59 \pm 0.06

TABLE VI
VIDEO GENERATION PERFORMANCE PER CFG WEIGHT.

CFG Scale (λ_{cfg})	Negative Condition	Dynamic (A4C)			Pediatric (A4C)			Pediatric (PSAX)			LVH (PLAX)		
		FID \downarrow	FVD \downarrow	IS \uparrow	FID \downarrow	FVD \downarrow	IS \uparrow	FID \downarrow	FVD \downarrow	IS \uparrow	FID \downarrow	FVD \downarrow	IS \uparrow
0.0	\emptyset	44.99	271.21	2.75 \pm 0.08	77.71	554.20	2.75 \pm 0.06	110.39	785.69	2.75 \pm 0.06	43.00	326.71	2.75 \pm 0.06
0.0	Anatomy	7.94	28.94	2.44 \pm 0.05	12.05	72.40	2.89 \pm 0.14	16.81	88.65	2.99 \pm 0.08	8.01	22.73	2.59 \pm 0.05
0.0	LVHF	45.47	277.85	2.75 \pm 0.07	76.70	553.17	2.74 \pm 0.03	108.90	770.57	2.75 \pm 0.05	40.39	301.29	2.73 \pm 0.06
1.0	N/A	7.92	28.1	2.46 \pm 0.06	12.26	75.4	2.88 \pm 0.14	16.77	84.6	2.99 \pm 0.09	7.71	23.2	2.58 \pm 0.06
2.0	\emptyset	5.62	51.07	2.49 \pm 0.06	8.61	65.41	2.91 \pm 0.19	10.43	62.87	3.15 \pm 0.11	5.44	38.79	2.58 \pm 0.11
2.0	Anatomy	8.07	28.57	2.47 \pm 0.06	11.93	71.65	2.92 \pm 0.15	16.14	85.21	3.09 \pm 0.11	7.59	22.27	2.57 \pm 0.07
2.0	LVHF	5.57	51.97	2.51 \pm 0.07	8.60	66.26	2.94 \pm 0.18	10.79	64.08	3.09 \pm 0.12	5.55	40.80	2.61 \pm 0.09
3.0	\emptyset	5.63	133.47	2.49 \pm 0.05	8.64	121.44	2.94 \pm 0.14	10.35	132.03	3.13 \pm 0.14	6.36	211.90	2.69 \pm 0.12
3.0	Anatomy	7.65	27.35	2.47 \pm 0.05	11.93	68.37	2.85 \pm 0.12	16.20	82.57	3.06 \pm 0.10	7.65	21.95	2.59 \pm 0.09
3.0	LVHF	5.90	138.80	2.51 \pm 0.08	8.56	126.21	2.95 \pm 0.16	10.42	131.16	3.20 \pm 0.13	6.47	217.02	2.63 \pm 0.10
4.0	\emptyset	6.00	217.35	2.48 \pm 0.08	8.48	198.08	2.93 \pm 0.14	10.68	192.71	3.17 \pm 0.09	6.65	365.51	2.66 \pm 0.09
4.0	Anatomy	7.59	27.22	2.50 \pm 0.06	13.04	68.25	2.91 \pm 0.15	15.74	80.70	3.05 \pm 0.10	7.42	22.34	2.58 \pm 0.06
4.0	LVHF	6.07	222.84	2.53 \pm 0.11	8.64	199.98	2.95 \pm 0.19	10.44	202.98	3.11 \pm 0.11	6.92	345.66	2.60 \pm 0.08
5.0	\emptyset	6.14	250.22	2.56 \pm 0.09	8.91	256.64	2.94 \pm 0.17	10.76	272.65	3.11 \pm 0.09	7.09	445.77	2.68 \pm 0.09
5.0	Anatomy	7.43	26.21	2.48 \pm 0.06	11.95	64.77	2.90 \pm 0.14	15.23	80.92	3.04 \pm 0.10	7.28	22.22	2.58 \pm 0.06
5.0	LVHF	6.26	262.29	2.52 \pm 0.09	9.20	257.50	2.92 \pm 0.19	10.61	257.38	3.15 \pm 0.14	6.96	450.39	2.65 \pm 0.08
10.0	\emptyset	7.14	200.20	2.59 \pm 0.06	9.78	266.35	2.92 \pm 0.16	11.58	297.65	3.09 \pm 0.09	7.34	416.93	2.72 \pm 0.07
10.0	Anatomy	7.31	25.36	2.51 \pm 0.04	11.66	59.93	2.91 \pm 0.14	14.47	71.00	3.12 \pm 0.13	6.75	21.43	2.59 \pm 0.08
10.0	LVHF	7.26	213.78	2.58 \pm 0.09	9.72	262.52	2.88 \pm 0.12	11.61	299.47	3.18 \pm 0.11	7.33	413.39	2.69 \pm 0.06

and projects it to a 1D vector of length 256. All four ReId models are configured with these parameters.

3) *Training*: We train one ReId model per dataset. The models are trained over latent space images and thus have very low compute requirements. Each model is trained for 50 000 steps, as the accuracy reaches 99% on the validation set. The learning rate is set to $1e-4$ and the batch size to 32.

4) *Evaluation*: After training the ReId models, we compute τ and apply each model on 100 000 latent images generated with the corresponding LIFM. For all datasets, the memorization rate is around 34%, as shown in Table V.

F. EchoFlow Dataset

For each dataset, we have identified the best A-VAE, LIFM and LVFM models. We have also trained ReId models on the corresponding real latent datasets. Putting things together, the LIFM generates 100 000 samples per dataset and we filter them with their corresponding ReId model. This gives us two sets of images, an unfiltered and a filtered one. To enable fair comparison with the real datasets, we randomly select synthetic images in the same quantities as the real datasets and respect the original splits sizes, as listed in Table VII. As such, we select the right amount of images from the unfiltered synthetic image collections for each dataset and split. Then, we duplicate these sets, remove any non-privacy compliant image, and replace them with unused privacy compliant images, forming our privacy-compliant sets. All images are then animated with the LVFM. We consider the average number of frames in each real dataset to decide how many times each anatomy should be animated to obtain a similar amount of frames per anatomy. As our video model generates 64-frame videos, we generate 3 videos per synthetic image for Dynamic and LVH, and 2 for Pediatrics. EF scores are randomly sampled in the range 10% – 90% and paired with a synthetic image.

In order to ensure the best possible results, we relabel every video with a pre-trained EF regression model. Each video gets

TABLE V
RE-IDENTIFICATION MODEL METRICS.

Dataset	LIFM Model	Threshold τ	Rejection rate
Dynamic	UNet-L-4f4	0.9997	35.8%
Pediatric (A4C)	UNet-L-4f4	0.9851	33.0%
Pediatric (PSAX)	FMT-L/2-4f4	0.9953	33.2%
LVH	FMT-L/2-4f4	0.9950	35.6%

TABLE VII
DATASETS SIZE AND SELECTED MODEL. A.F.C STANDS FOR ‘AVERAGE FRAME COUNT’.

Dataset	LIFM Model	LVFM Model	Train	Val.	Test	A.F.C.
Dynamic	UNet-L-4f4	FMvT-S/2-4f4	7465	1288	1277	177
Pediatric (A4C)	UNet-L-4f4	FMvT-S/2-4f4	2580	336	368	101
Pediatric (PSAX)	FMT-L/2-4f4	FMvT-S/2-4f4	3559	448	519	103
LVH	FMT-L/2-4f4	FMvT-S/2-4f4	9508	1076	332	165

TABLE VIII
DOWNSTREAM TASKS PERFORMANCE.

	Dynamic (A4C)			Pediatric (A4C)			Pediatric (PSAX)			LVH (PLAX)		
	R2 \uparrow	MAE \downarrow	RMSE \downarrow	R2 \uparrow	MAE \downarrow	RMSE \downarrow	R2 \uparrow	MAE \downarrow	RMSE \downarrow	R2 \uparrow	MAE \downarrow	RMSE \downarrow
Claimed	0.81	4.05	5.32	0.70	4.15	5.70	0.74	3.80	5.14	–	–	–
Reproduced	0.81	3.98	5.29	0.68	4.19	5.71	0.71	3.79	5.14	0.55	6.42	8.38
A-VAE-4f4 Rec.	0.81	4.08	5.38	0.70	4.65	6.37	0.68	4.21	5.95	0.57	6.43	8.21
A-VAE-16f8 Rec.	0.81	3.99	5.28	0.68	4.57	6.52	0.70	4.12	5.78	0.58	6.36	8.13
EchoDiff. [43]	0.55	6.02	8.21	–	–	–	–	–	–	–	–	–
EchoSyn. [44]	0.75	4.55	6.10	0.70	5.06	7.07	0.68	4.82	6.95	–	–	–
EchoFlow (NPC)	0.81	4.10	5.40	0.72	4.08	6.10	0.73	3.92	5.48	0.53	6.62	8.60
EchoFlow (PC)	0.81	4.05	5.34	0.72	4.29	6.09	0.72	3.95	5.60	0.55	6.54	8.34

attributed this new EF score as its label. This is done to correct approximations introduced by the LVFM model.

By following these steps, we generate a total of 8 video collections: a non-privacy-compliant (NPC) and a privacy-compliant (PC) synthetic version of each original dataset.

G. Evaluation on Downstream Tasks

We compare the performance of an EF regression model trained on various datasets in Table VIII. We report the results claimed in each dataset’s original work (‘Claimed’) and the results we obtained from reproducing said work (‘Reproduced’) row. We then explore the impact of training the regression model on datasets reconstructed with our A-VAEs and observe no performance degradation compared to the Reproduced results. For the synthetic datasets, we compare our datasets (EchoFlow) with existing baselines (EchoDiff. [43] and EchoSyn. [44]). In a controlled and fair setting, our new synthetic datasets outperform all previous approaches and reach performance parity with the real datasets, even on the privacy-preserving synthetic datasets.

V. CONCLUSION

In this work, we introduced a comprehensive framework for generating high-fidelity, privacy-preserving cardiac ultrasound images and videos. By leveraging generative modelling techniques, such as Adversarial Variational Auto-Encoders for domain-specific latent space construction, Latent Flow Matching for both image and video generation, and a robust Re-Identification mechanism for privacy filtering, we demonstrated that privacy preserving, synthetic medical imaging

datasets can achieve performance parity with real data in downstream clinical tasks like EF regression. Our extensive experiments across multiple datasets (including EchoNet-Dynamic, EchoNet-Pediatric, and EchoNet-LVH) reveal that scaling model size and training time effectively closes the quality and diversity gap between real and synthetic samples. This work not only paves the way for broader data sharing in medical imaging without compromising patient privacy but also establishes a solid foundation for future research in generative models across diverse clinical applications.

REFERENCES

- [1] Arjovsky, M., et al.: Wasserstein generative adversarial networks. In: International conference on machine learning. pp. 214–223. PMLR (2017)
- [2] Black Forest Labs: Flux.1-dev, <https://huggingface.co/black-forest-labs/FLUX.1-dev>
- [3] Blattmann, A., et al.: Align your latents: High-resolution video synthesis with latent diffusion models. In: CVPR (2023)
- [4] Blattmann, A., et al.: Stable video diffusion: Scaling latent video diffusion models to large datasets. arXiv:2311.15127 (2023)
- [5] Brock, A., et al.: Large scale GAN training for high fidelity natural image synthesis. In: ICLR (2019)
- [6] Brooks, T., et al.: Instructpix2pix: Learning to follow image editing instructions. In: CVPR (2023)
- [7] Cao, T., et al.: Don't generate me: Training differentially private generative models with sinkhorn divergence. NeurIPS **34**, 12480–12492 (2021)
- [8] Carlini, N., et al.: Extracting training data from diffusion models. In: USENIX Security. pp. 5253–5270 (2023)
- [9] Chen, L.C., et al.: Rethinking atrous convolution for semantic image segmentation. arXiv preprint arXiv:1706.05587 (2017)
- [10] Chen, T., et al.: Ultrasound image-to-video synthesis via latent dynamic diffusion models. In: MICCAI. pp. 764–774. Springer (2024)
- [11] Chen, Y., et al.: Generative ai in medical practice: in-depth exploration of privacy and security challenges. JMIR **26**, e53008 (2024)
- [12] Child, R.: Very deep vae generalizes autoregressive models and can outperform them on images. In: ICLR (2021)
- [13] Dar, S.U.H., et al.: Unconditional latent diffusion models memorize patient imaging data. arXiv:2402.01054 (2024)
- [14] Dhariwal, P., et al.: Diffusion models beat gans on image synthesis. NeurIPS **34** (2021)
- [15] Dombrowski, M., et al.: Quantifying sample anonymity in score-based generative models with adversarial fingerprinting (2023)
- [16] Esser, P., et al.: Scaling rectified flow transformers for high-resolution image synthesis. In: ICML (2024)
- [17] Gilbert, A., et al.: Generating synthetic labeled data from existing anatomical models: an example with echocardiography segmentation. TMI **40**(10), 2783–2794 (2021)
- [18] Goodfellow, I., et al.: Generative adversarial networks. NeurIPS **27** (2014)
- [19] He, Y., et al.: Latent video diffusion models for high-fidelity video generation with arbitrary lengths. arXiv:2211.13221 (2022)
- [20] Ho, J., et al.: Denoising Diffusion Probabilistic Models. In: NeurIPS. vol. 33, pp. 6840–6851 (2020)
- [21] Ho, J., et al.: Classifier-Free Diffusion Guidance (jul 2022), arXiv:2207.12598
- [22] Ho, J., et al.: Imagen Video: High Definition Video Generation with Diffusion Models (oct 2022), arXiv:2210.02303
- [23] Ho, J., et al.: Video Diffusion Models (jun 2022), arXiv:2204.03458
- [24] Huang, Z., et al.: Tmed 2: A dataset for semi-supervised classification of echocardiograms. In: DataPerf workshop at ICML (2022)
- [25] Jensen, J.: Simulation of advanced ultrasound systems using Field II. In: ISBI. pp. 636–639 Vol. 1 (may 2004)
- [26] Jin, Y., et al.: Pyramidal flow matching for efficient video generative modeling. In: ICLR (2025)
- [27] Khachatryan, L., et al.: Text2video-zero: Text-to-image diffusion models are zero-shot video generators. In: ICCV (oct 2023)
- [28] Kingma, D.P., et al.: Auto-Encoding Variational Bayes. In: ICLR (2014)
- [29] Kumari, N., et al.: Multi-concept customization of text-to-image diffusion. arXiv:2212.04488 (2022)
- [30] Lee, S., et al.: Improving the training of rectified flows. In: NeurIPS (2024)
- [31] Li, Y., et al.: Echopulse: Ecg controlled echocardiograms video generation. arXiv:2410.03143 (2024)
- [32] Liang, J., et al.: Sketch guided and progressive growing GAN for realistic and editable ultrasound image synthesis. Medical Image Analysis **79**, 102461 (jul 2022)
- [33] Lipman, Y., et al.: Flow matching for generative modeling. In: ICLR (2023)
- [34] Ma, X., et al.: Latte: Latent diffusion transformer for video generation. arXiv preprint arXiv:2401.03048 (2024)
- [35] Nguyen, V.P., et al.: Training-free condition video diffusion models for single frame spatial-semantic echocardiogram synthesis. In: MICCAI. pp. 670–680. Springer (2024)
- [36] Ouyang, D., et al.: Video-based AI for beat-to-beat assessment of cardiac function. Nature **580**, 252–256 (may 2020)
- [37] Peebles, W., et al.: Scalable diffusion models with transformers. In: ICCV (2023)
- [38] Rajpurkar, P., et al.: Ai in health and medicine. Nature Medicine pp. 1–8 (2022)
- [39] Rakhimov, R., et al.: Latent video transformer. arXiv:2006.10704 (2020)
- [40] Reddy, C.D., et al.: Video-based deep learning for automated assessment of left ventricular ejection fraction in pediatric patients. JASE **36**(5), 482–489 (2023)
- [41] Reynaud, H., et al.: Ultrasound Video Transformers for Cardiac Ejection Fraction Estimation. In: MICCAI. pp. 495–505. Springer (2021)
- [42] Reynaud, H., et al.: D'ARTAGNAN: Counterfactual Video Generation. In: MICCAI. pp. 599–609. Springer (2022)
- [43] Reynaud, H., et al.: Feature-Conditioned Cascaded Video Diffusion Models for Precise Echocardiogram Synthesis. In: MICCAI. pp. 142–152. Springer (2023)
- [44] Reynaud, H., et al.: Echonet-synthetic: Privacy-preserving video generation for safe medical data sharing. In: MICCAI. pp. 285–295. Springer (2024)
- [45] Rombach, R., et al.: High-Resolution Image Synthesis with Latent Diffusion Models (may 2022), arXiv:2112.10752
- [46] Ronneberger, O., et al.: U-Net: Convolutional Networks for Biomedical Image Segmentation (may 2015), arXiv:1505.04597
- [47] Rueckert, D., et al.: Learning clinically useful information from images: Past, present and future (2016)
- [48] Saharia, C., et al.: Photorealistic Text-to-Image Diffusion Models with Deep Language Understanding (may 2022), arXiv:2205.11487
- [49] Schlemper, J., et al.: Attention gated networks: Learning to leverage salient regions in medical images. Medical image analysis **53**, 197–207 (2019)
- [50] Shams, R., et al.: Real-Time Simulation of Medical Ultrasound from CT Images. In: MICCAI. pp. 734–741. Springer (2008)
- [51] Singer, U., et al.: Make-A-Video: Text-to-Video Generation without Text-Video Data (sep 2022), arXiv:2209.14792
- [52] StabilityAI: Stable diffusion 2-1 (2022), <https://huggingface.co/stabilityai/stable-diffusion-2-1>
- [53] StabilityAI: Stable diffusion v1-4 (2022), <https://huggingface.co/CompVis/stable-diffusion-v1-4>
- [54] StabilityAI: Stable diffusion 3.5 large (2024), <https://huggingface.co/stabilityai/stable-diffusion-3.5-large>
- [55] Stanford University: EchoNet-LVH Dataset (2020), <https://doi.org/10.71718/wtrx-wj56>
- [56] Stojanovski, D., et al.: Echo from noise: synthetic ultrasound image generation using diffusion models for real image segmentation. In: MICCAI ASMUS Workshop. pp. 34–43. Springer (2023)
- [57] Teichholz, L.E., et al.: Problems in echocardiographic volume determinations: echocardiographic-angiographic correlations in the presence or absence of asynergy. American journal of cardiology **37**(1), 7–11 (1976)
- [58] Teng, L., et al.: Interactive Translation in Echocardiography Training System With Enhanced Cycle-GAN. IEEE Access **8**, 106147–106156 (2020)
- [59] Tiago, C., et al.: A data augmentation pipeline to generate synthetic labeled datasets of 3d echocardiography images using a gan. IEEE Access **10**, 98803–98815 (2022)
- [60] Tomar, D., et al.: Content-Preserving Unpaired Translation from Simulated to Realistic Ultrasound Images. In: MICCAI. pp. 659–669 (2021)
- [61] Van Den Oord, A., et al.: Pixel recurrent neural networks. In: ICML. p. 1747–1756 (2016)
- [62] Vaswani, A., et al.: Attention is all you need. NeurIPS (2017)
- [63] Yu, K.H., et al.: Artificial intelligence in healthcare. Nature Biomedical Engineering p. 719–731 (2018)
- [64] Zhou, X., et al.: Heartbeat: Towards controllable echocardiography video synthesis with multimodal conditions-guided diffusion models. In: MICCAI. pp. 361–371. Springer (2024)